https://doi.org/10.5194/essd-2022-200
Preprint. Discussion started: 1 September 2022

Open Access Earth System Science Data Discussions

A dataset of standard precipitation index reconstructed from multi-proxies over Asia for the past 300 years

Yang Liu[1], Jingyun Zheng[1,2], Zhixin Hao[1,2], Quansheng Ge[1,2]

[1] Key Laboratory of Land Surface Pattern and Simulation, Institute of Geographic Sciences and Natural Resources Research, Chinese Academy of Sciences, Beijing 100101, China
[2] College of Resources and Environment, University of Chinese Academy of Sciences, Beijing 100049, China

Correspondence to: Jingyun Zheng (zhengjy@igsnrr.ac.cn); Quansheng Ge (geqs@igsnrr.ac.cn)

Abstract. Proxy-based precipitation reconstruction is essential to study the inter-annual to decadal variability and underlying mechanisms beyond the instrumental period that is critically needed for climate modeling, prediction, and attribution. Based on 3014 annually resolved proxy series mainly derived from tree-ring and historical documents, we present a set of standard precipitation index (SPI) reconstructions for annual (Nov-Oct) covering entire Asia and for wet season (i.e., Nov-Apr for western Asia and May-Oct for the others) with the spatial resolution of 2.5° since 1700. To screen the optimal candidate proxies for SPI reconstruction in each grid from available proxies in its connected region with a homogeneous rainfall regime and similar precipitation variability, a new approach is develop by adopting the grid-location-dependent division derived from the instrumental SPI data. The validation shows that these reconstructions are effective for most of Asia. The assessment of data quality compared with gauge precipitation before calibration time indicates that our reconstruction has high quality to show the precipitation variability in most of the study areas except for few grids in western Russia, the coastal area of southeastern Asia and northern Japan.

1 Introduction

Asia bears the brunt of flood and drought disasters associated with extensive social and economic damages than any other continent due to its large and heterogeneous landmass, plus high population densities in the south and east regions (Cred and Unisdr, 2015). However, the inter-annual, decadal and centennial spatiotemporal variability of Asian precipitation and underlying mechanisms have not been fully characterized, which limits the performance of precipitation projection for the next decades to hundred years. Long-term, spatially-resolved, and high-quality precipitation datasets are needed to address these issues. Unfortunately, the global precipitation observation network only covers the past century (Sun et al., 2018) while the data for the first half period in Asia is also at low confidence levels (Hartmann et al., 2013). Therefore, proxy-based precipitation reconstructions are essential to quantify the precipitation variability beyond the instrumental period.

Up to now, there are four gridded datasets to reconstruct summer (or the warm season) precipitation variability in mid-low latitude Asia for the past hundreds of years (Cook et al., 2010a; Feng et al., 2013; Shi et al., 2018; Shi et al., 2017), by

https://doi.org/10.5194/essd-2022-200
Preprint. Discussion started: 1 September 2022

using tree-ring chronologies only or merging multi-proxies. For example, using 327 tree-ring chronologies mainly located in the Tibetan Plateau and Mongolia, Cook et al. (2010a) reconstructed the gridded (2.5° × 2.5°) summer (Jun–Aug, JJA) Palmer drought severity index (PDSI) over Monsoon Asia during 1300-2005. By weighted merging 453 tree-ring-width chronologies and 71-site dryness/wetness grade series derived from Chinese historical documents (local gazettes), Shi et al. (2018) reconstructed a gridded Asian summer precipitation dataset for 1470-2013. Similar reconstructions were also conducted for North America (Cook et al., 2010b; Stahle et al., 2020), Europe (Cook et al., 2015; Cook et al., 2020), and Oceania (Palmer et al., 2015). Moreover, by using a data assimilation (DA) approach to combine 2978 proxy data with the physical constraints of the atmosphere-ocean climate model together, a globally gridded (2.0° × 2.0°) hydroclimate index dataset over the Common Era was also reconstructed (Steiger et al., 2018), including PDSI and the standardized precipitation evapotranspiration index (SPEI) for JJA, DJF (Dec-Feb) and April to the next March. These datasets extend records back in time and provide valuable efforts on improving the gridded paleoclimate reconstruction by synthesizing multi-proxy from individual sites with spatiotemporal inhomogeneity.

However, intercomparisons of the abovementioned four gridded precipitation variability reconstructions in monsoon Asia (Cook et al., 2010a; Feng et al., 2013; Shi et al., 2018; Shi et al., 2017) with independent instrumental observation data show notable differences among them caused by proxies and methods for calibration, particularly dominated by the number and sample distribution of proxies used, as well as the seasonal sensitivity of the individual proxy to precipitation anomaly (Liu et al., 2021). For example, in the reconstruction only from tree-ring proxies, the explained variance in regions with spars proxies (e.g., eastern China, Indochina Peninsula) is usually less than 20% (Cook et al, 2010a). By merging tree-ring and documentary proxies in the reconstruction, the result is believed to illustrate large-scale rainfall variability faithfully but has more uncertainties in representing regional rainfall anomalies (Shi et al., 2018). Moreover, the precipitation over Asia has a complex spatial pattern with the temporal variability on intra-seasonal and inter-annual scales (Hsu et al., 2014) due to different rainfall regimes in space (Awan et al., 2015; Conroy and Overpeck, 2011). Therefore, the sensitivity of individual proxy to precipitation anomaly has evident regional differences for seasons. In addition, many new proxies achieved in recent years are not utilized in the above-mentioned four gridded reconstructions in monsoon Asia. All of these motivate us to initiate this new gridded (2.5° × 2.5°) reconstruction effort on seasonal to annual precipitation variability in Asia.

2 Data and Method

2.1 The study area and the framework for grid SPI reconstruction

The spatial coverage of our reconstruction is Asia plus Russian territory in Europe (Fig. 1), and the reconstructed target is standard precipitation index (SPI) based on multi-proxies by calibrating with monthly instrumental gridded SPI data. In this vast study area, there are many climatic types with heterogeneous precipitation, specifically, the wet season in western Asia and the southwest part of central Asia is mainly from November to April (Nov-Apr), but that in the rest regions is May-October (May-Oct) due to different rainfall regimes in different regions (Bombardi et al., 2019; Peng et al., 2020). Thus, we

https://doi.org/10.5194/essd-2022-200
Preprint. Discussion started: 1 September 2022

reconstructed the annual (November to October, Nov-Oct) SPI for the entire study area, as well as the Nov-Apr SPI in western Asia and the southwest part of central Asia and the May-Oct SPI in the other regions for the wet season, respectively. Moreover, there exists a complex spatial coherence pattern for the precipitation variation on scales of inter-annual, decadal and longer in the study area, which means the spatial representativeness of the individual proxy is dominated by the location in the context of the region (e.g., shape and area) with coherent rainfall regime and variation. Therefore, we develop a new approach to select proxies for each grid SPI reconstruction by adopting the grid-location-dependent division (GLDD) derived from the instrumental SPI data, instead of selecting proxies usually from an isotropic search radius for all grids in many previous studies (e.g., Cook et al., 2010a; Shi et al., 2018).

2.2 Instrumental data for calibration and spatial pattern of wet season identification

In our study, the grid size for SPI reconstruction is set as 2.5° ×2.5 °. The instrumental data used for calibration is resized from the 0.5° ×0.5 ° gridded monthly SPI data for 1948-2019 calculated by NOAA’s land precipitation product (Chen et al., 2002), which was downloaded via IRI/LDEO Climate Data Library (http://iridl.ldeo.columbia.edu/SOURCES/.IRI/.Analyses/.SPI/). As pointed out by the previous studies (Bombardi et al., 2019; Peng et al., 2020), the wet season in Asia could be roughly classified as two terms of Nov-Apr and May-Oct. Therefore, to identify the spatial pattern of the wet season for SPI reconstruction in the 2.5° ×2.5 ° gridded scale induced by different regional rainfall regimes, the monthly precipitation data for 1948-2019 by GPCC (Schneider et al., 2017) is also used to calculate two consecutive months with the most rainfall amount in a year (Fig. 1). It is shown that in most parts of the study area, the wettest two consecutive months are in May-Oct. However, in western Asia (excluding the south corner of the Arabian Peninsula), the southwest part of central Asia, and the tropical zone south to 10 °N, the wettest two consecutive months are in Nov-Apr. Moreover, there also exists a few grids (dot marked in Fig. 1) that have no distinct wet season. Thus, we exclude the dotted grids in wet season SPI reconstruction.

2.3 Proxy data preparing

There are a total of 3014 annually resolved proxy series from Asia and adjacent land areas (Eastern Europe and Alaska) for reconstruction, of which 2899 are derived from tree-ring, 110 from historical documents, 4 from ice cores, and 1 from a stalagmite. Their spatial and temporal distribution is shown in Fig. 2. Noted that all of the proxy series have at least ten records in the calibration period to ensure a sufficient sample size for the regression. The data source and standardized processes for each type of proxy series are described below.

Tree-ring data are mainly from the International Tree Ring Data Bank (ITRDB), maintained by the World Data Center for Paleoclimatology (WDC-P, https://www.ncei.noaa.gov/products/paleoclimatology). Most sites have two categories of data, i.e., original raw tree-ring measurements and tree-ring index chronologies derived from raw measurements. However, the index chronologies are not used directly in this study because they were standardized by various methods which are not

https://doi.org/10.5194/essd-2022-200
Preprint. Discussion started: 1 September 2022

described in the online metadata and some of the common methods may result in a substantial loss of long-term fluctuations (Coulthard et al., 2020). To maximally preserve the climatic related low-frequency variance, we recalculate the chronologies from raw measurements by removing the growth trend with age-dependent splines (Melvin et al., 2007). In a few cases where age-dependent splines contain zeros or negative values, a more flexible curve, Friedman variable span smoother (Friedman, 1984), is used to fit the growth trend. In addition, some trees experience disturbances during their lifespan, which could cause abrupt growth increases or reductions (Altman, 2020). To eliminate this effect, the running mean technique (Altman et al., 2014) is applied to identify the disturbance event then separate growth curves are fitted before and after this year. Finally, the 51-year sliding expressed population signal (EPS) is calculated and the threshold of 0.85 is used to determine the first reliable year of a chronology. The above procedures are also applied for sites with raw measurements only. For the other 32 sites that only have chronologies, EPS is not available thus we use the minimum sample size of 5 to determine the first reliable year. Besides ITRDB, 16 tree-ring chronologies that indicate local precipitation or drought from recently published papers are included in our study (Shah et al., 2007; Sass-Klaassen et al., 2008; Arsalani et al., 2018; Arsalani et al., 2015; Chen et al., 2016; Zhang et al., 2017; Pumijumnong et al., 2020; Xu et al., 2015; Buckley et al., 2017; Ukhvatkina et al., 2021; Akkemik et al., 2020; Kostyakova et al., 2017; Kucherov, 2010). Compared with the tree-ring network used in previous studies over the monsoon Asia region (Cook et al., 2010a; Feng et al., 2013; Shi et al., 2018; Shi et al., 2017), a total of 135 ring-width chronologies are added in our study.

It is worth noting that the total 2899 tree-ring proxies consist both of width and density chronologies in part of sites. According to the principle of dendroclimatology, the availability of soil water affects the growth rate and formation of wood, both within a season and the longer terms (Vaganov et al., 2011), tree-ring width chronologies used for precipitation reconstruction should have significant positive correlations with the target variable and tree-ring density chronologies should be excluded because they are usually correlated with temperature variation (Wettstein et al., 2011; Briffa et al., 2002). Thus, only the tree-ring width chronologies positively correlated to precipitation are selected as the candidate proxy for our SPI reconstruction. However, due to multiple types of climate and complex topography in the vast study area, the tree-ring density chronologies and width chronologies with negative correlations to precipitation may also well indicate precipitation variation indirectly (Wettstein et al., 2011; George, 2014). Therefore, we also conduct an alternative reconstruction based on all tree-ring chronologies of width and density for comparison.

The proxy from historical documents is mainly the dryness/wetness grade series for 120 sites in China for the past 500 years (henceforth referred to as DW120) (Cma, 1981). The grades were calibrated based on descriptions of drought/flood and their impacts during the wet season mainly recorded in Chinese local gazettes using ideal frequency criteria of all time, roughly 10% for grades 1 and 5 (heavy flood and severe drought), 20-30% for grades 2 and 4 (flood and drought), and 30-40% for grade 3 (normal). This grade dataset originally ended in 1979 (Cma, 1981) and was extended to 2000 (Zhang et al., 2003; Zhang and Liu, 1993), which becomes an essential dataset to reconstruct summer precipitation over the Asia monsoon domain (Feng et al., 2013; Shi et al., 2018; Shi et al., 2017). However, DW120 contains a large proportion of missing data because there are only 26040 grade records since 1700 (Fig. 3a), which limits the spatial and temporal coverage of data for grid SPI reconstruction. Therefore, we update this dataset by two supplementary ways. Firstly, Zhang (1996) also reconstructed a dryness/wetness grade dataset that contains 65 sites in central eastern China (DW65) by following the same grading criteria as DW120. Although DW65 has 65 sites only, it had fewer missing records because it was reconstructed by more abundant historical documents (such as the drought/flood descriptions recorded in the memoirs and archives of the Qing Dynasty). Therefore, we add the missing 2045 records of DW120 from DW65. Secondly, DW120 provides an isoline map for individual years when most sites have available data (Cma, 1981). Therefore, the missing data could be interpolated from isolines, which supplements 4121 grade records in total. This updated DW120 finally contains 32206 grade records since 1700, which has a 23.7% increase compared with the original version (Fig. 3b). Unfortunately, no data are available before the 20th century for 10 sites in west China and one site in northeast China (cross marked in Fig. 3b), thus only 109 sites in China are selected for our SPI reconstruction. Another documentary-based proxy is the dryness/wetness grade series since 1781 in Mumbai, India, which also consists of 5 grades calibrated against the percentage of rainfall anomaly derived from instrumental data in their overlapped period (Adamson and Nash, 2014).

In addition, the rest of the hydro-climatic proxy series derived from 4 ice cores in the Himalayas and one stalagmite in India, are also downloaded from WDC-P. It is worth noting that the stable oxygen isotope ($\delta^{18}O$) ratio series of the ice core from East Rongbuk Glacier is unequally spaced with a mean temporal resolution of 0.082 years, which is simply re-sampled to an annual resolved series by averaging data in the same year.

2.4 Method for grid SPI calibration and validation

Since the proxies are uneven distributed in space and time, we use best subset regression (BSR) to screen optimal combinations of the candidate proxies for calibration in each grid SPI reconstruction based on available proxies in different intervals respectively, in which the candidate proxies are selected by the GLDD approach. Here shows the Nov-Oct SPI reconstruction for a grid centered at 91.25 °E and 28.75 °N (located in southwest China) as an example for the detailed steps.

Firstly, calculating the spatial SPI correlation field of the target grid and identifying the regions with positively significant ($p<0.05$) correlation coefficients (Fig. 4a). It shows that the target grid and its adjacent grids have significant correlations that cover an irregular shape (i.e., not a circle-like with isotropic radius from the target grid or other regular shape) in southwest China, which means there exists robust coherence for SPI variation. This is because the rainfall regime and precipitation for that region are usually dominated by the same atmospheric circulation systems (Zhang and Wang, 2021). Besides, there are some other remote regions (e.g., the Malay Archipelago, Russian Plain, and regions around New Siberian Islands) that show significant correlations to the target grid. However, prior studies had reported that the long-distance precipitation teleconnection patterns are usually unstable through a long-term period since they are linked by large-scale atmospheric circulations or propagating waves (Wu, 2016; Boers et al., 2019). Therefore, the candidate proxies for the target grid SPI reconstruction should be searched only from the connected region (called "searching region" hereafter, Fig. 4b), and there are a total of 43 proxies for the candidate proxy selection.

https://doi.org/10.5194/essd-2022-200
Preprint. Discussion started: 1 September 2022

Secondly, calculating the correlations between the target grid SPI and each series of 43 proxies in the searching region to select the candidate proxy by the threshold of the 0.1 significance level for the correlations. Note that prior summer precipitation could affect the tree-ring formation in the next year (Wettstein et al., 2011), thus 1-year lagged tree-ring chronologies are also included for the Nov-Oct SPI reconstruction. However, the proxies with highly positive correlations may lead to multi-linearity effects in the regression equation for calibration. Thus, we also calculate the correlations among all 43 proxy series, and if any pair of proxy series shows an extremely high positive correlation (i.e., $r > 0.90$ and $p < 0.0001$) in their common period, the shorter one will be excluded from the pool of candidate proxies. By this step, a total of 8 proxy series (including 5 tree-ring width series, 1 tree-ring $\delta^{18}O$ series, and 2 dryness/wetness grade series) are selected for BSR in the following step (Fig. 4b).

Thirdly, establishing the calibration equation by using BSR for each time segment depends on the length of the candidate proxy series. According to the start and end year of all 8 candidate proxy series, the time of proxy availability should be classified into 6 segments, in which there are 8 candidate proxies for 1772-1998, 7 candidate proxies for 2 segments in 1745-1772 and 1998-2000 respectively, 6 candidate proxies for 1743-1745, 5 candidate proxies for 1739-1743, and 4 candidate proxies for 1700-1939 (Fig. 4c). Moreover, to avoid the overfitting in the regression induced by redundant independent variables (Lever et al., 2016), if there are more than 5 candidate proxies, only 5 proxy series with top 5 significant levels for the correlations with target SPI are retained for the regression. Thus, 3 individual segments (1743-1945, 1745-1772 and 1972-1998) retain the same 5 proxies (i.e., two tree-ring width series, one tree-ring $\delta^{18}O$ series and two DW120 series), and they could be regarded as one segment of 1943-1998. Then, we use BSR to establish 4 calibration equations for SPI reconstruction in 1700-1739, 1740-1942, 1943-1998, 1998-2000 respectively, in which the best subset selection is determined by maximizing the adjusted coefficient of determination (R^2a). Finally, the target SPI series for the full time is constructed by merging the reconstructions for individual segments. As the reconstructions for different segments were calibrated from different equations with different variances and predicted sums of squares, the magnitudes of the reconstructed SPI for a specific segment had to be adjusted using the variance matching method with respect to the standard deviations of the predictands in common years during the calibration period (Mccarroll et al., 2015).

We calculate two commonly used statistical parameters in climate reconstruction for validation, coefficient of efficiency (CE) and reduction of error (RE) (Cook et al., 1994). Considering that the temporal coverage of our calibration data is 1948 to present, we applied the leave-one-out (LOO) method to conduct cross-validation. Consequently, the equations for RE and CE are calculated as:

$$\mathrm{RE} = 1 - \left[\frac{\sum(\hat{y}_{icv} - y_i)^2}{\sum(y_i - \bar{y}_{icv})^2}\right] \quad (1)$$

$$\mathrm{CE} = 1 - \left[\frac{\sum(\hat{y}_{icv} - y_i)^2}{\sum(y_i - \bar{y}_{cv})^2}\right] \quad (2)$$

https://doi.org/10.5194/essd-2022-200
Preprint. Discussion started: 1 September 2022

where y_i is the actual data in year i, $\hat{y}_{icv}$ is the estimated data in year i by LOO, $\bar{y}_{icv}$ is the mean of actual data excluding y_i and $\bar{y}_{cv}$ is the mean of actual data in the cross-validation period. All the three skill metrics, R^2a, RE and CE, are expressions of fractional explained variance to the actual data while CE is generally more stringent than the other two.

3 Results and discussion

The dataset of includes 4 SPI reconstructions: (1) the Nov-Oct SPI reconstruction for entire Asia without using tree-ring density chronologies and width chronologies with negative correlations to precipitation (Nov-Oct SPI Version A); (2) the Nov-Oct SPI reconstruction for entire Asia by adding tree-ring density chronologies and width chronologies with negative correlations to precipitation (Nov-Oct SPI Version B); (3) the wet season SPI reconstruction for the extra-tropical Asia (Nov-Apr SPI for western Asia and May-Oct SPI for the rest regions) without using tree-ring density chronologies and width chronologies with negative correlations to precipitation (wet season SPI Version A); (4) the wet season SPI reconstruction for the extra-tropical Asia (Nov-Apr SPI for western Asia and May-Oct SPI for the rest regions) by adding tree-ring density chronologies and width chronologies with negative correlations to precipitation (wet season SPI Version B). Each of them is stored in a MATLAB formatted binary file (.mat) and contains a structure named recon that has 5 three-dimension (longitude × latitude × time) variables, including reconstructed SPI, calibration R^2, calibration R^2a, validation RE, and validation CE.

3.1 Validity of the reconstruction

Figures 5 show the spatial patterns of R^2a, RE and CE for the Nov-Oct SPI reconstruction since 1700 by a 50-year interval. It shows that CE in the most of study areas is positive. Although few grids have negative CE, especially before 1800, most of them still have positive RE. These results mean the reconstruction is effective, in which the area with $R^2a > 0.2$ accounts for 41.2% of grids in Asia in 1700, and extends to 68.2% in 1950 due to more and more available proxies. Since 1700, the areas with $R^2a > 0.4$ are distributed in a board region from the southwest coast of the Caspian Sea to Balkhash Lake to eastern China, and some grids in the northern Far East, northern India and western Indochina Peninsula. R^2a gradually passed 0.4 from 1750 to 1800 over Turkey, West Siberian Plain, central Asia, Mongolia and India. The highest R^2a (more than 0.6) appeared in central eastern China throughout the entire 300-year period.

By adding tree-ring density chronologies and width chronologies with negative correlations to precipitation in the Nov-Oct SPI reconstruction (i.e. Version B), the number of grid with ineffective reconstruction is significantly reduced and the R^2a for most of the grids is significantly increased (Fig. 6). Compare to the Nov-Oct SPI reconstruction Version A (Fig. 5), the area with $R^2a > 0.2$ in Version B accounts for 67.4% of grids in Asia in 1700, and extends to 87.2% in 1950. In particular, R^2a increases by 0.2~0.3 in central to eastern Russia and by 0.1 to 0.2 in other regions except for the Arabian Peninsula and eastern China.

Likewise, for the wet season SPI reconstruction, it is also effective in most grids (Fig. 7), in which the area with $R^2a >$ 0.2 accounts for 42.5% of grids in Asia in 1700, and extends to 64.4% in 1950. Compared with the Nov-Oct SPI Version A

https://doi.org/10.5194/essd-2022-200
Preprint. Discussion started: 1 September 2022

(Fig. 5), the wet season SPI reconstruction shows significantly higher R^2a (0.1-0.2) for the region on the east of the Caspian Sea, slightly higher R^2a (around 0.1) for most grids in high latitude zone, while a reduced R^2a around 0.1 in eastern China. For the wet season SPI reconstruction by adding tree-ring density chronologies and width chronologies with negative correlations to precipitation, the percentage of area with $R^2a > 0.2$ in 1700 and 1950 is 65.7% and 87.3%, respectively (Fig. 8). The difference in skill metrics between two wet season SPI versions (Fig. 7 and 8) is similar to that between two Nov-Oct SPI versions (Fig. 5 and 6).

3.2 Data quality and usability

Compare to three reconstructions of summer (June-August or May-September) precipitation (or PDSI) in monsoon Asia by previous studies (Cook et al., 2010a; Feng et al., 2013; Shi et al., 2018), the R^2a in the calibration period of our May-Oct SPI reconstructions (Fig. 7p and Fig. 8p) are 10% higher than that of the best one in three reconstructions over south Tibetan Plateau to eastern India subcontinent, western Indochina peninsula and northwest China. Moreover, our reconstruction has a slightly higher R^2a in parts of Mongolia, central Asia and eastern China than that in other reconstructions. In particular, R^2a in eastern China in our reconstruction is about 40% higher than that from the reconstruction only by tree-ring data (Cook et al., 2010a). These improvements are not only because more proxy data (including the DWI derived from Chinese historical documents and the tree-ring data published recently) are added, but also because the development of the reconstruction method that selects proxies by the GLDD approach from a connected searching region with significantly positive correlations to the target grid SPI.

To further assess the quality of reconstructed data, we compare our Nov-Oct SPI reconstruction with gauge precipitation at those weather stations with at least 30-year records before 1948, in which the precipitation data is from the Global Historical Climatology Network monthly (GHCNm, 2022) dataset version 2 and Long-Term Instrumental Climatic Data Bases of the People's Republic of China (Tao et al., 1997). We calculate the correlations between Nov-Oct precipitation anomaly percentage and Nov-Oct SPI reconstruction in corresponding grids (Fig. 9). The result shows that the correlations for most sites, especially in eastern and southern Asia, pass the significant level of 0.1, though the correlation is not significant for part sites in central Asia, western Asia, the coastal area in southeastern Asia and western Russia. For example, in the 6-sites (Haerbin, Beijing, Qingdao, Shanghai, Yichang and Shantou) evenly distributed across eastern China (Fig. 9), all the correlations between reconstruction and observation pass the 0.01 significant level (Fig. 10). Moreover, the reconstructions could reproduce the most of extreme years, e.g., 1853, 1871, 1890, 1893, 1920 and 1921 in Beijing, 1875, 1876, 1889, 1891, 1892, 1921, 1929, 1931 and 1934 in Shanghai, and 1889, 1897, 1900, 1902, 1920, 1928, 1935 and 1937 in Yichang (Fig. 10). This assessment indicates that our reconstruction has high quality to show the precipitation variability in most of the study areas except for few grids in western Russia, the coastal area of southeastern Asia and northern Japan. Thus, these datasets could be used to further study the spatiotemporal variability and underlying mechanisms of Asian precipitation since the pre-industrial era that is critically needed for climate modeling, prediction, and attribution.

https://doi.org/10.5194/essd-2022-200
Preprint. Discussion started: 1 September 2022

4 Data availability

The dataset can be accessed from https://www.scidb.cn/en/s/26jQ3i (Liu et al., 2022). This dataset is licensed under a CC BY 4.0 license.

5 Conclusions

In this study, we use a multi-proxy (mainly from tree-ring and historical documents with clear annual dating) network containing 3014 series to reconstruct SPI for the wet season (Nov-Apr for west Asia and May-Oct for the others) and annual (Nov-Oct) time scale since 1700 over Asia with the spatial resolution of 2.5 ° × 2.5 °. Compare to the previous studies (Cook et al., 2010a; Feng et al., 2013; Shi et al., 2018; Shi et al., 2017), our reconstruction is conducted at the grid level by calibration method, which could search proxies for a target grid by a new approach of GLDD from its connected areas within a sub-region having homogeneous rainfall regime and similar precipitation variability. Meanwhile, many new proxies were used, mainly including additional 135 tree-ring width chronologies in the monsoon Asia and more than 6100 dry/wet grade data (23.7%) from historical documents in China. These additional proxies evidently improve the coverage and distribution of proxies, and their temporal homogeneity due to the reconstructed period being limited to 300 years only. This dataset is the first SPI reconstruction covering entire Asia based on pure proxies (without long-term observations or climate model constraints) and can be used to more clearly investigate the Asian precipitation change since 1700, and to test the paleoclimate simulation in the industrial period.

Author contributions

QG and JZ designed the study and planned the reconstructions. YL processed the experimental data, performed the computations and drafted the manuscript. JZ critically revised the manuscript. All authors discussed and contributed to the reconstruction and manuscript.

Competing interests

The authors declare that they have no conflict of interest.

Acknowledgements

This work was supported by the National Key R&D Program of China on Global change (2017YFA0603300) and the National Natural Science Foundation of China (42005043, 42175058). We acknowledge the World Data Center for

https://doi.org/10.5194/essd-2022-200
Preprint. Discussion started: 1 September 2022

Paleoclimatology (WDC-P, https://www.ncei.noaa.gov/products/paleoclimatology) for hosting and providing paleoclimatology database.

References

Adamson, G. C. D. and Nash, D. J.: Documentary reconstruction of monsoon rainfall variability over western India, 1781-1860, Clim. Dyn., 42, 749-769, 2014.
Akkemik, Ü., Köse, N., Kopabayeva, A., and Mazarzhanova, K.: October to July precipitation reconstruction for Burabai region (Kazakhstan) since 1744, International Journal of Biometeorology, 64, 803-813, 10.1007/s00484-020-01870-8, 2020.
Altman, J., Fibich, P., Dolezal, J., and Aakala, T.: TRADER: A package for Tree Ring Analysis of Disturbance Events in R, Dendrochronologia, 32, 107-112, 10.1016/j.dendro.2014.01.004, 2014.
Altman, J.: Tree-ring-based disturbance reconstruction in interdisciplinary research: Current state and future directions, Dendrochronologia, 63, 10.1016/j.dendro.2020.125733, 2020.
Arsalani, M., Azizi, G., and Bräuning, A.: Dendroclimatic reconstruction of May-June maximum temperatures in the central Zagros Mountains, western Iran, Int. J. Climatol., 35, 408-416, 10.1002/joc.3988, 2015.
Arsalani, M., Pourtahmasi, K., Azizi, G., Bräuning, A., and Mohammadi, H.: Tree-ring based December–February precipitation reconstruction in the southern Zagros Mountains, Iran, Dendrochronologia, 49, 45-56, 10.1016/j.dendro.2018.03.002, 2018.
Awan, J. A., Bae, D. H., and Kim, K. J.: Identification and trend analysis of homogeneous rainfall zones over the East Asia monsoon region, Int. J. Climatol., 35, 1422-1433, 2015.
Boers, N., Goswami, B., Rheinwalt, A., Bookhagen, B., Hoskins, B., and Kurths, J.: Complex networks reveal global pattern of extreme-rainfall teleconnections, Nature, 566, 373-377, 10.1038/s41586-018-0872-x, 2019.
Bombardi, R. J., Kinter, J. L., and Frauenfeld, O. W.: A Global Gridded Dataset of the Characteristics of the Rainy And Dry Seasons, Bull. Am. Meteorol. Soc., 100, 1315-1328, 10.1175/bams-d-18-0177.1, 2019.
Briffa, K. R., Osborn, T. J., Schweingruber, F. H., Jones, P. D., Shiyatov, S. G., and Vaganov, E. A.: Tree-ring width and density data around the Northern Hemisphere: Part 1, local and regional climate signals, Holocene, 12, 737-757, 2002.
Buckley, B. M., Stahle, D. K., Luu, H. T., Wang, S. Y. S., Nguyen, T. Q. T., Thomas, P., Le, C. N., Ton, T. M., Bui, T. H., and Nguyen, V. T.: Central Vietnam climate over the past five centuries from cypress tree rings, Clim. Dyn., 48, 3707-3723, 10.1007/s00382-016-3297-y, 2017.
Chen, F., Mambetov, B., Maisupova, B., and Kelgenbayev, N.: Drought variations in Almaty (Kazakhstan) since AD 1785 based on spruce tree rings, Stoch. Environ. Res. Risk Assess., 31, 2097-2105, 10.1007/s00477-016-1290-y, 2016.
Chen, M., Xie, P., Janowiak, J. E., and Arkin, P. A.: Global Land Precipitation: A 50-yr Monthly Analysis Based on Gauge Observations, J. Hydrometeorol., 3, 249-266, 10.1175/1525-7541(2002)003<0249:Glpaym>2.0.Co;2, 2002.
CMA: Yearly charts of dryness/wetness for the last 500-year period, SinoMaps Press, Beijing1981.
Conroy, J. L. and Overpeck, J. T.: Regionalization of Present-Day Precipitation in the Greater Monsoon Region of Asia, J. Clim., 24, 4073-4095, 10.1175/2011jcli4033.1, 2011.
Cook, E. R., Anchukaitis, K. J., Buckley, B. M., D'Arrigo, R. D., Jacoby, G. C., and Wright, W. E.: Asian Monsoon Failure and Megadrought During the Last Millennium, Science, 328, 486-489, 10.1126/science.1185188, 2010a.
Cook, E. R., Briffa, K. R., and Jones, P. D.: Spatial regression methods in dendroclimatology: A review and comparison of two techniques, Int. J. Climatol., 14, 379-402, 10.1002/joc.3370140404, 1994.
Cook, E. R., Seager, R., Heim, R. R., Vose, R. S., Herweijer, C., and Woodhouse, C.: Megadroughts in North America: placing IPCC projections of hydroclimatic change in a long-term palaeoclimate context, J. Quat. Sci., 25, 48-61, 10.1002/jqs.1303, 2010b.
Cook, E. R., Seager, R., Kushnir, Y., Briffa, K. R., Büntgen, U., Frank, D., Krusic, P. J., Tegel, W., van der Schrier, G., Andreu-Hayles, L., Baillie, M., Baittinger, C., Bleicher, N., Bonde, N., Brown, D., Carrer, M., Cooper, R., Čufar, K., Dittmar, C., Esper, J., Griggs, C., Gunnarson, B., Günther, B., Gutierrez, E., Haneca, K., Helama, S., Herzig, F., Heussner, K.-U., Hofmann, J., Janda, P., Kontic, R., Köse, N., Kyncl, T., Levanič, T., Linderholm, H., Manning, S., Melvin, T. M., Miles, D., Neuwirth, B., Nicolussi, K., Nola, P., Panayotov, M., Popa, I., Rothe, A., Seftigen, K., Seim, A., Svarva, H., Svoboda, M., Thun, T., Timonen, M., Touchan, R., Trotsiuk,

https://doi.org/10.5194/essd-2022-200
Preprint. Discussion started: 1 September 2022

V., Trouet, V., Walder, F., Ważny, T., Wilson, R., and Zang, C.: Old World megadroughts and pluvials during the Common Era, Science Advances, 1, 10.1126/sciadv.1500561, 2015.

Cook, E. R., Solomina, O., Matskovsky, V., Cook, B. I., Agafonov, L., Berdnikova, A., Dolgova, E., Karpukhin, A., Knysh, N., Kulakova, M., Kuznetsova, V., Kyncl, T., Kyncl, J., Maximova, O., Panyushkina, I., Seim, A., Tishin, D., Dotny, T. W. O., and Yermokhin, M.: The European Russia Drought Atlas (1400-2016 CE), Clim. Dyn., 54, 2317-2335, 2020.

Coulthard, B. L., St. George, S., and Meko, D. M.: The limits of freely-available tree-ring chronologies, Quat. Sci. Rev., 234, 10.1016/j.quascirev.2020.106264, 2020.

CRED and UNISDR: The Human Cost of Weather-Related Disasters 1995-2015, Centre for Research on the Epidemiology of Disasters and United Nations International Strategy for Disaster Reduction, Brussels and Geneva, 30, 2015.

Feng, S., Hu, Q., Wu, Q. R., and Mann, M. E.: A Gridded Reconstruction of Warm Season Precipitation for Asia Spanning the Past Half Millennium, J. Clim., 26, 2192-2204, 10.1175/JCLI-D-12-00099.1, 2013.

Friedman, J. H.: A variable span smoother, Department of Statistics, Stanford University, Stanford, CASLAC-PUB-3477, 30, 10.2172/1447470, 1984.

George, S. S.: An overview of tree-ring width records across the Northern Hemisphere, Quat. Sci. Rev., 95, 132-150, 10.1016/j.quascirev.2014.04.029, 2014.

GHCNm (Global Historical Climatology Network monthly): https://www.ncei.noaa.gov/products/land-based-station/global-historical-climatology-network-monthly, last access: 2022-05-20.

Hartmann, D. L., Klein Tank, A. M. G., Rusticucci, M., Alexander, L. V., Brönnimann, S., Charabi, Y., Dentener, F. J., Dlugokencky, E. J., Easterling, D. R., Kaplan, A., Soden, B. J., Thorne, P. W., Wild, M., and Zhai, P. M.: Observations: Atmosphere and Surface, in: Climate Change 2013: The Physical Science Basis. Contribution of Working Group I to the Fifth Assessment Report of the Intergovernmental Panel on Climate Change, edited by: Stocker, T. F., Qin, D., Plattner, G.-K., Tignor, M., Allen, S. K., Boschung, J., Nauels, A., Xia, Y., Bex, V., and Midgley, P. M., Cambridge University Press, Cambridge, United Kingdom and New York, NY, USA, 159–254, 10.1017/CBO9781107415324.008, 2013.

Hsu, H. H., Zhou, T. J., and Matsumoto, J.: East Asian, Indochina and Western North Pacific Summer Monsoon - An update, Asia-Pac J Atmos Sci, 50, 45-68, 10.1007/s13143-014-0027-4, 2014.

Kostyakova, T. V., Touchan, R., Babushkina, E. A., and Belokopytova, L. V.: Precipitation reconstruction for the Khakassia region, Siberia, from tree rings, The Holocene, 28, 377-385, 10.1177/0959683617729450, 2017.

Kucherov, S. E.: Reconstruction of summer precipitation in the Southern Urals over the last 375 years based on analysis of radial increment in the Siberian larch, Russian Journal of Ecology, 41, 284-292, 10.1134/s1067413610040028, 2010.

Lever, J., Krzywinski, M., and Altman, N.: Model selection and overfitting, Nature Methods, 13, 703-704, 10.1038/nmeth.3968, 2016.

Liu, Y., Hao, Z. X., Zhang, X. Z., and Zheng, J. Y.: Intercomparisons of multiproxy-based gridded precipitation datasets in Monsoon Asia: cross-validation and spatial patterns with different phase combinations of multidecadal oscillations, Clim. Change, 165, 31, 10.1007/s10584-021-03072-6, 2021.

Liu, Y., Zheng, J., Hao, Z., and Ge, Q.: A dataset of standard precipitation index reconstructed from multi-proxies over Asia for the past 300 years, Science Data Bank [dataset], doi:10.57760/sciencedb.01829, 2022.

McCarroll, D., Young, G. H. F., and Loader, N. J.: Measuring the skill of variance-scaled climate reconstructions and a test for the capture of extremes, The Holocene, 25, 618-626, 10.1177/0959683614565956, 2015.

Melvin, T. M., Briffa, K. R., Nicolussi, K., and Grabner, M.: Time-varying-response smoothing, Dendrochronologia, 25, 65-69, 10.1016/j.dendro.2007.01.004, 2007.

Palmer, J. G., Cook, E. R., Turney, C. S. M., Allen, K., Fenwick, P., Cook, B. I., O'Donnell, A., Lough, J., Grierson, P., and Baker, P.: Drought variability in the eastern Australia and New Zealand summer drought atlas (ANZDA, CE 1500–2012) modulated by the Interdecadal Pacific Oscillation, Environ Res Lett, 10, 10.1088/1748-9326/10/12/124002, 2015.

Peng, D. D., Zhou, T. J., and Zhang, L. X.: Moisture Sources Associated with Precipitation during Dry and Wet Seasons over Central Asia, J. Clim., 33, 10755-10771, 10.1175/Jcli-D-20-0029.1, 2020.

Pumijumnong, N., Brauning, A., Sano, M., Nakatsuka, T., Muangsong, C., and Buajan, S.: A 338-year tree-ring oxygen isotope record from Thai teak captures the variations in the Asian summer monsoon system, Sci. Rep., 10, 8966, 2020.

Sass-Klaassen, U., Leuschner, H. H., Buerkert, A., and Helle, G.: Tree-ring analysis of Juniperus excelsa from the northern Oman mountains, Proceedings of the Dendrosymposium 2007, Riga, Latvia2008.

https://doi.org/10.5194/essd-2022-200
Preprint. Discussion started: 1 September 2022

Schneider, U., Finger, P., Meyer-Christoffer, A., Rustemeier, E., Ziese, M., and Becker, A.: Evaluating the Hydrological Cycle over Land Using the Newly-Corrected Precipitation Climatology from the Global Precipitation Climatology Centre (GPCC), Atmosphere-Basel, 8, 52, 10.3390/atmos8030052, 2017.

Shah, S. K., Bhattacharyya, A., and Chaudhary, V.: Reconstruction of June–September precipitation based on tree-ring data of teak (Tectona grandis L.) from Hoshangabad, Madhya Pradesh, India, Dendrochronologia, 25, 57-64, 10.1016/j.dendro.2007.02.001, 2007.

Shi, F., Zhao, S., Guo, Z. T., Goosse, H., and Yin, Q. Z.: Multi-proxy reconstructions of May-September precipitation field in China over the past 500 years, Clim Past, 13, 1919-1938, 10.5194/cp-13-1919-2017, 2017.

Shi, H., Wang, B., Cook, E. R., Liu, J., and Liu, F.: Asian Summer Precipitation over the Past 544 Years Reconstructed by Merging Tree Rings and Historical Documentary Records, J. Clim., 31, 7845-7861, 10.1175/Jcli-D-18-0003.1, 2018.

Stahle, D. W., Cook, E. R., Burnette, D. J., Torbenson, M. C. A., Howard, I. M., Griffin, D., Diaz, J. V., Cook, B. I., Williams, A. P., Watson, E., Sauchyn, D. J., Pederson, N., Woodhouse, C. A., Pederson, G. T., Meko, D., Coulthard, B., and Crawford, C. J.: Dynamics, Variability, and Change in Seasonal Precipitation Reconstructions for North America, J. Clim., 33, 3173-3195, 10.1175/jcli-d-19-0270.1, 2020.

Steiger, N. J., Smerdon, J. E., Cook, E. R., and Cook, B. I.: Data Descriptor: A reconstruction of global hydroclimate and dynamical variables over the Common Era, Sci Data, 5, 2018.

Sun, Q. H., Miao, C. Y., Duan, Q. Y., Ashouri, H., Sorooshian, S., and Hsu, K. L.: A Review of Global Precipitation Data Sets: Data Sources, Estimation, and Intercomparisons, Rev. Geophys., 56, 79-107, 10.1002/2017RG000574, 2018.

Tao, S., Fu, C., Zeng, Z., and Zhang, Q.: Two Long-Term Instrumental Climatic Data Bases of the People's Republic of China (NDP039) [dataset], 10.3334/CDIAC/cli.ndp039, 1997.

Ukhvatkina, O., Omelko, A., Kislov, D., Zhmerenetsky, A., Epifanova, T., and Altman, J.: Tree-ring-based spring precipitation reconstruction in the Sikhote-Alin' Mountain range, Clim. Past, 17, 951-967, 10.5194/cp-17-951-2021, 2021.

Vaganov, E. A., Anchukaitis, K. J., and Evans, M. N.: How Well Understood Are the Processes that Create Dendroclimatic Records? A Mechanistic Model of the Climatic Control on Conifer Tree-Ring Growth Dynamics, in: Dendroclimatology, edited by: Hughes, M. K., Swetnam, T. W., and Diaz, H. F., Developments in Paleoenvironmental Research, 37-75, 10.1007/978-1-4020-5725-0_3, 2011.

Wettstein, J. J., Littell, J. S., Wallace, J. M., and Gedalof, Z. e.: Coherent Region-, Species-, and Frequency-Dependent Local Climate Signals in Northern Hemisphere Tree-Ring Widths, J. Clim., 24, 5998-6012, 10.1175/2011JCLI3822.1, 2011.

Wu, R.: Relationship between Indian and East Asian summer rainfall variations, Adv. Atmos. Sci., 34, 4-15, 10.1007/s00376-016-6216-6, 2016.

Xu, C., Pumijumnong, N., Nakatsuka, T., Sano, M., and Li, Z.: A tree-ring cellulose δ18O-based July–October precipitation reconstruction since AD 1828, northwest Thailand, J. Hydrol., 529, 433-441, 10.1016/j.jhydrol.2015.02.037, 2015.

Zhang, D. e. and Liu, C.: Continuation (1980-1992) of the "Yearly Charts of Dryness/ Wetness in China for the last 500-Years Period", Meteorological Monthly, 19, 41-45, 1993.

Zhang, D. e., Li, X., and Liang, Y.: Continuation (1992-2000) of the "Yearly Charts of Dryness/Wetness in China for the Last 500-Years Period", Quarterly Journal of Applied Meteorology, 14, 379-388, 2003.

Zhang, P. Y.: Climate Change in China during Historical Times, Shandong Science and Technology Press, Jinan1996.

Zhang, R. B., Shang, H. M., Yu, S. L., He, Q., Yuan, Y. J., Bolatov, K., and Mambetov, B. T.: Tree-ring-based precipitation reconstruction in southern Kazakhstan, reveals drought variability since AD 1770, Int. J. Climatol., 37, 741-750, 2017.

Zhang, Y. and Wang, K.: Global precipitation system size, Environ Res Lett, 16, 10.1088/1748-9326/abf394, 2021.

https://doi.org/10.5194/essd-2022-200
Preprint. Discussion started: 1 September 2022

Figure captions

Figure 1: The study area and the spatial difference of rainfall regime with the wettest bimester (two consecutive months) shown by the monthly GPCP precipitation data from 1948-2019. The dot marker indicates that the grid lacks a clear wet season. Annual (Nov-Oct) SPI is reconstructed for all non-grey grids, while wet season (Nov-Apr and May-Oct) SPI is reconstructed in regions with black and brown boundaries respectively.

Figure 2: Spatial (a) and temporal (b) distribution of proxies.

Figure 3: Proportion of available data for DW120 in original version (a) and after updating (b). Sites with a cross marker in (b) are excluded in reconstruction.

Figure 4: Demonstration of a grid SPI reconstruction for showing proxy-selecting by the GLDD approach. (a) The target grid (yellow square) and regions (light blue) that have significantly (at least $p<0.05$) positive correlated SPI change. (b) The searching region connected with the target grid and proxies in it. A proxy marker with a black edge means it is significantly (at least p<0.1) correlated with SPI change in the target grid. (c) Temporal coverage of picked proxy series and derived four segments based on available proxies. Proxies are listed in ascending order of *p*-value from bottom to top. When a segment has more than 5 proxies, the bottom 5 (solid patch) are used in BSR and the others (cross patch) are excluded. Proxies remain in the final BSR model are marked with plus signs. (d) Reconstructed SPI series and calibration R^2a for each segment.

Figure 5: R^2a, RE, and CE for Nov-Oct SPI reconstruction by multi-proxies without using tree-ring density chronologies and width chronologies with negative correlations to precipitation.

Figure 6: R^2a, RE, and CE for Nov-Oct SPI reconstruction by multi-proxies including tree-ring density chronologies and width chronologies with negative correlations to precipitation.

Figure 7: R^2a, RE, and CE for wet season SPI reconstruction by multi-proxies without using tree-ring density chronologies and width chronologies with negative correlations to precipitation, the black line indicates the boundary of the region in which the wet season is Nov-Apr as that in Fig. 1.

Figure 8: R^2a, RE, and CE for wet season SPI reconstruction by multi-proxies including tree-ring density chronologies and width chronologies with negative correlations to precipitation, the black line indicates the boundary of the region in which the wet season is Nov-Apr as that in Fig. 1.

https://doi.org/10.5194/essd-2022-200
Preprint. Discussion started: 1 September 2022

Figure 9: Correlations between Nov-Oct precipitation anomaly percentage for weather stations with at least 30-year records before 1948 from GHCMm and Nov-Oct SPI reconstruction in corresponding grids. The six selected sites in eastern China are shown with black edges, and the comparisons between observation and reconstruction year by year in these sites will be shown as the examples in Fig. 10.

Figure 10: Comparisons between Nov-Oct precipitation anomaly percentage for 6 sites across eastern China from Tao et al. (1997) and Nov-Oct SPI reconstruction in corresponding grids. (a) Haerbin (126.62 °E, 45.68 °N), (b) Beijing (116.28 °E, 39.93 °N), (c) Qingdao (120.33 °E, 36.07 °N), (d) Shanghai (121.43 °E, 31.17 °N), (e) Yichang (111.30 °E, 30.70 °N), and (f) Shantou (116.68 °E, 23.40 °N). Their locations are also shown in Fig. 9.

https://doi.org/10.5194/essd-2022-200
Preprint. Discussion started: 1 September 2022

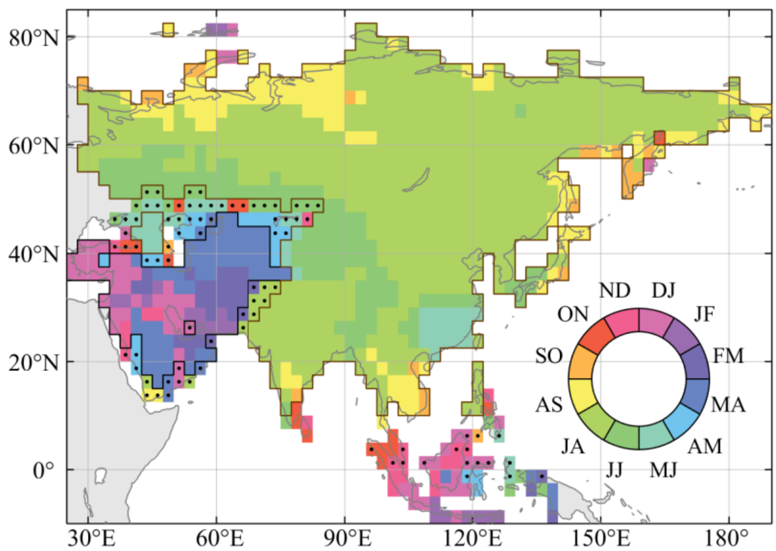

Figure 1: The study area and the spatial difference of rainfall regime with the wettest bimester (two consecutive months) shown by the monthly GPCP precipitation data from 1948-2019. The dot marker indicates that the grid lacks a clear wet season. Annual (Nov-Oct) SPI is reconstructed for all non-grey grids, while wet season (Nov-Apr and May-Oct) SPI is reconstructed in regions with black and brown boundaries respectively.

https://doi.org/10.5194/essd-2022-200
Preprint. Discussion started: 1 September 2022

Open Access Earth System Science Data Discussions

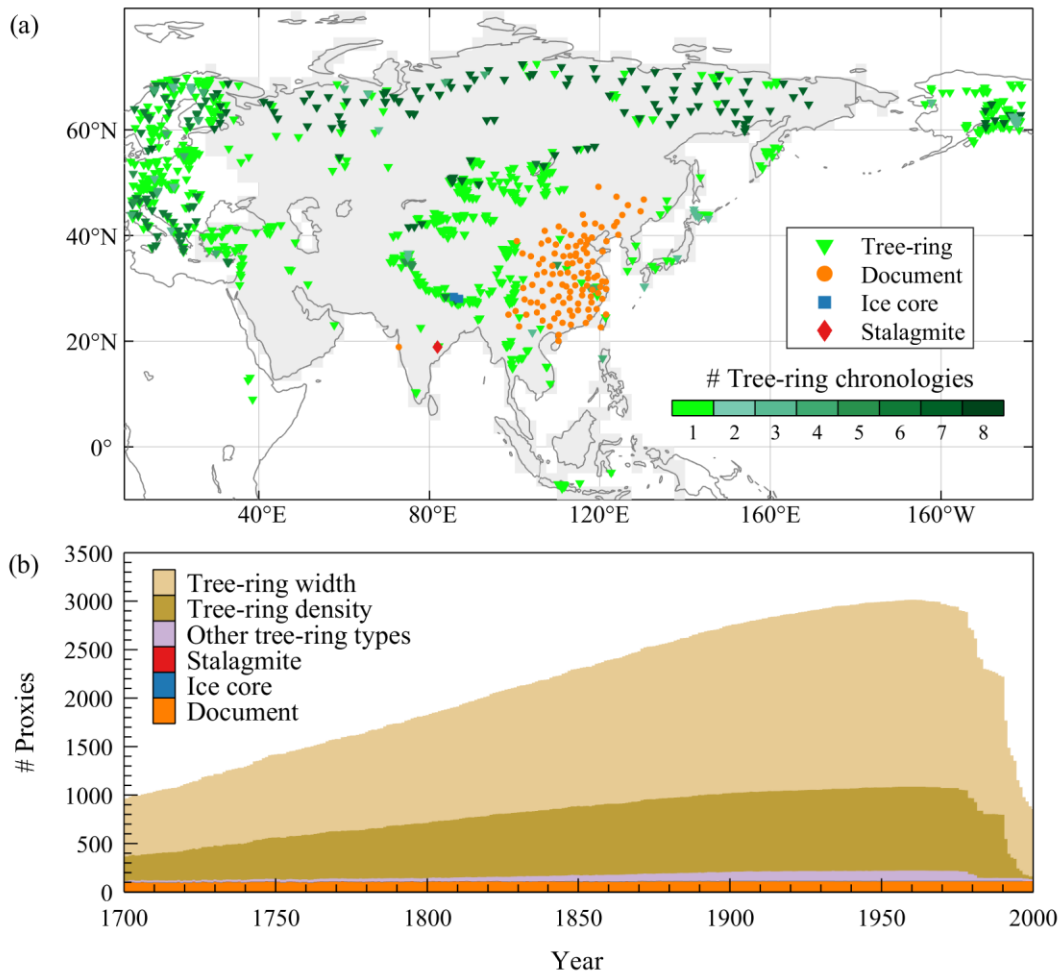

Figure 2: Spatial (a) and temporal (b) distribution of proxies.

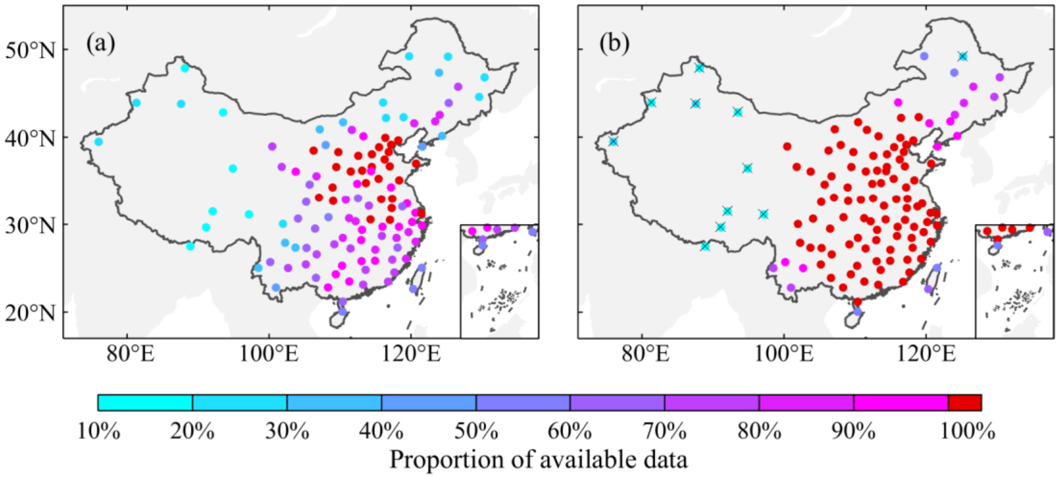

Figure 3: Proportion of available data for DW120 in original version (a) and after updating (b). Sites with a cross marker in (b) are excluded in reconstruction.

https://doi.org/10.5194/essd-2022-200
Preprint. Discussion started: 1 September 2022

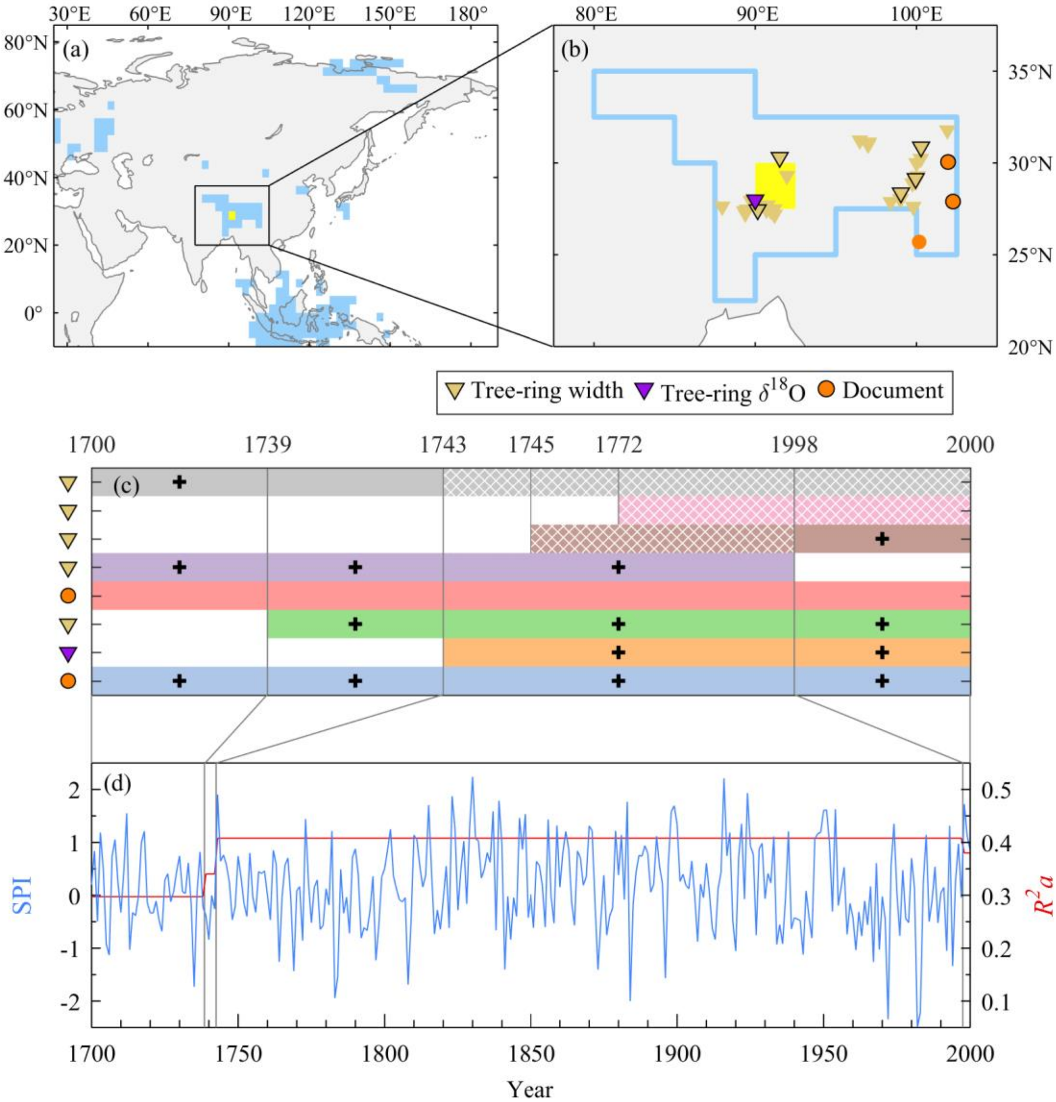

Figure 4: Demonstration of a grid SPI reconstruction for showing proxy-selecting by the GLDD approach. (a) The target grid (yellow square) and regions (light blue) that have significantly (at least $p<0.05$) positive correlated SPI change. (b) The searching region connected with the target grid and proxies in it. A proxy marker with a black edge means it is significantly (at least p<0.1) correlated with SPI change in the target grid. (c) Temporal coverage of picked proxy series and derived four segments based on available proxies. Proxies are listed in ascending order of p-value from bottom to top. When a segment has more than 5 proxies, the bottom 5 (solid patch) are used in BSR and the others (cross patch) are excluded. Proxies remain in the final BSR model are marked with plus signs. (d) Reconstructed SPI series and calibration R^2a for each segment.

https://doi.org/10.5194/essd-2022-200
Preprint. Discussion started: 1 September 2022

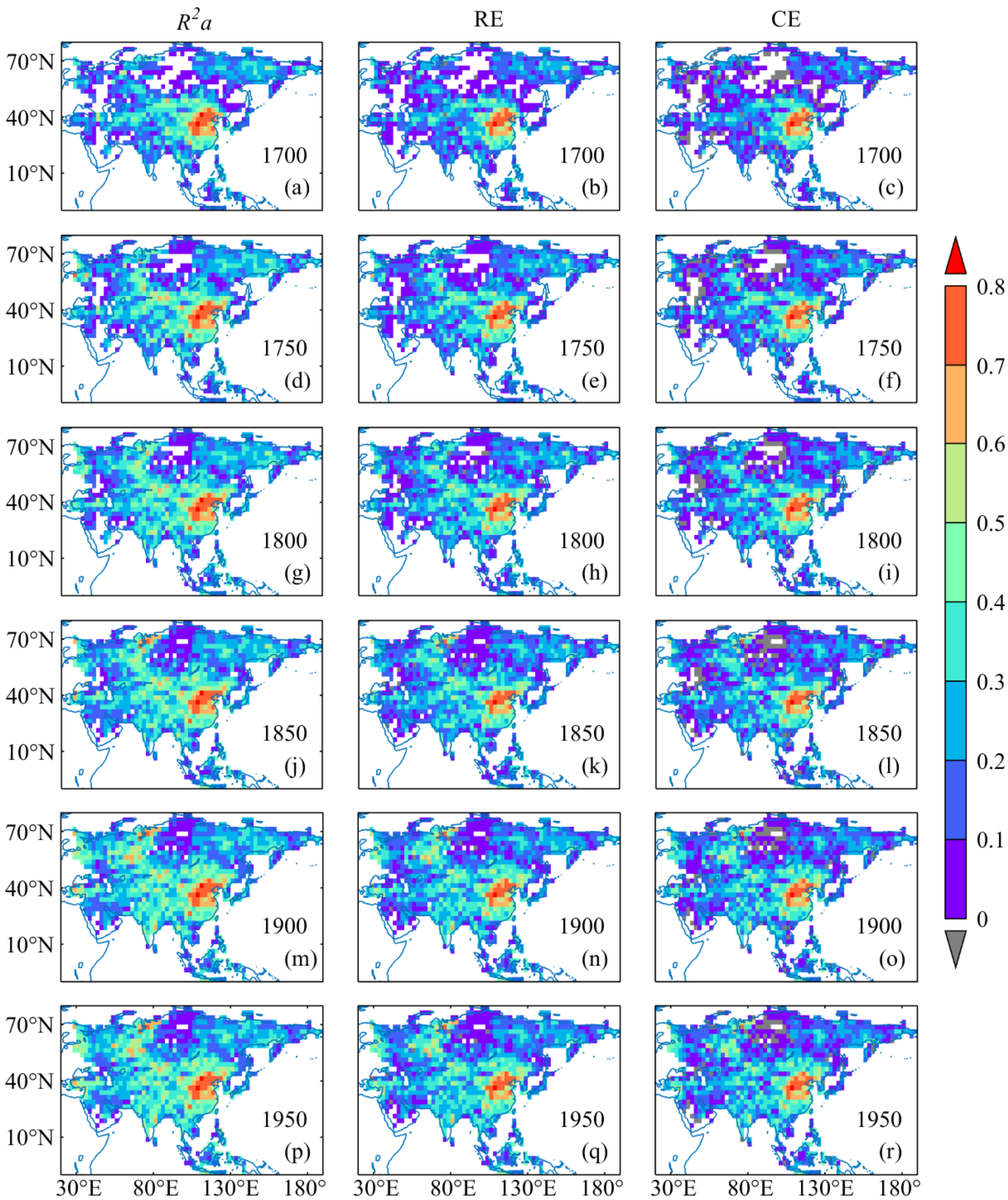

Figure 5: R^2a, RE, and CE for Nov-Oct SPI reconstruction by multi-proxies without using tree-ring density chronologies and width chronologies with negative correlations to precipitation.

https://doi.org/10.5194/essd-2022-200
Preprint. Discussion started: 1 September 2022

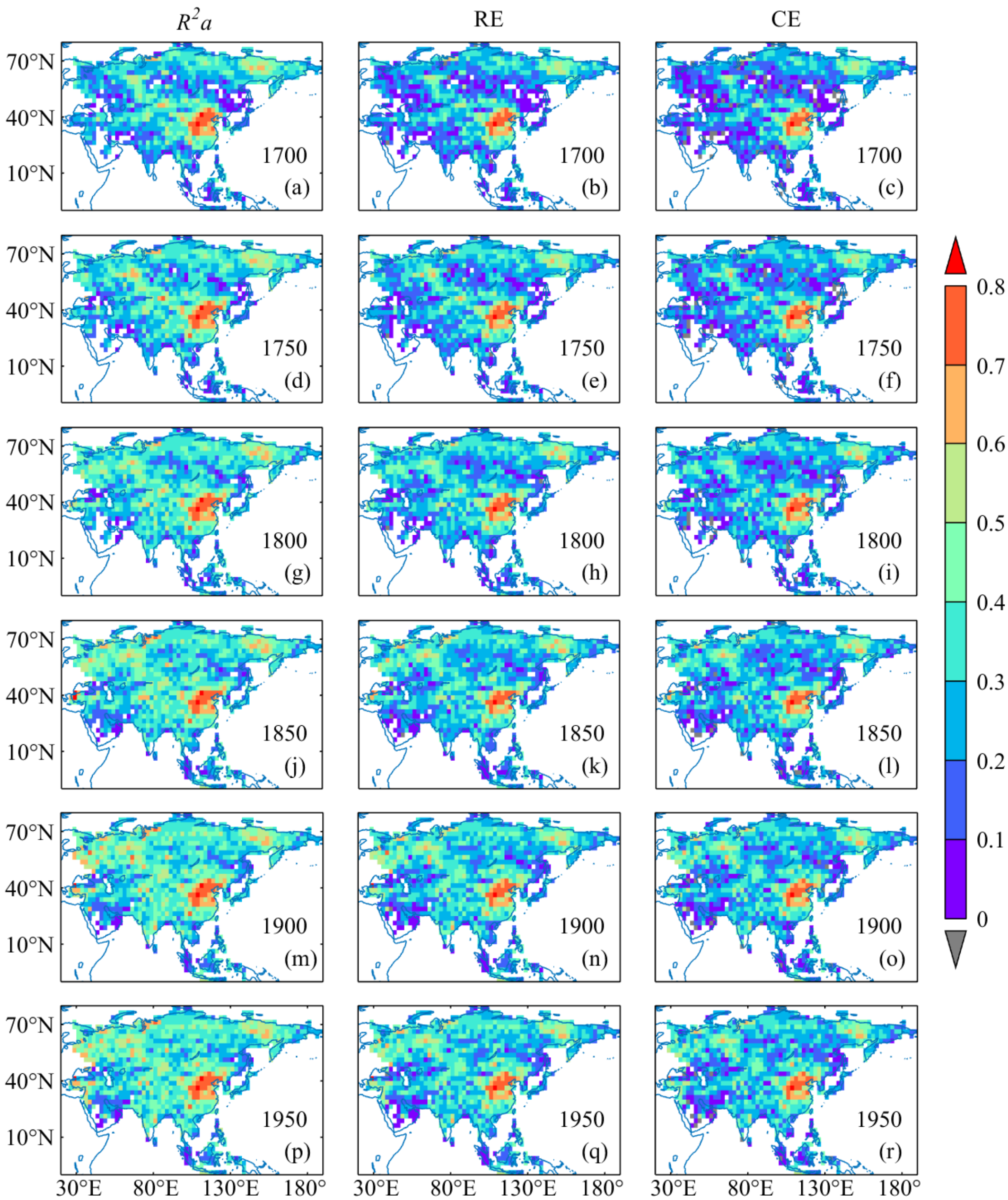

Figure 6: R^2a, RE, and CE for Nov-Oct SPI reconstruction by multi-proxies including tree-ring density chronologies and width chronologies with negative correlations to precipitation.

https://doi.org/10.5194/essd-2022-200
Preprint. Discussion started: 1 September 2022

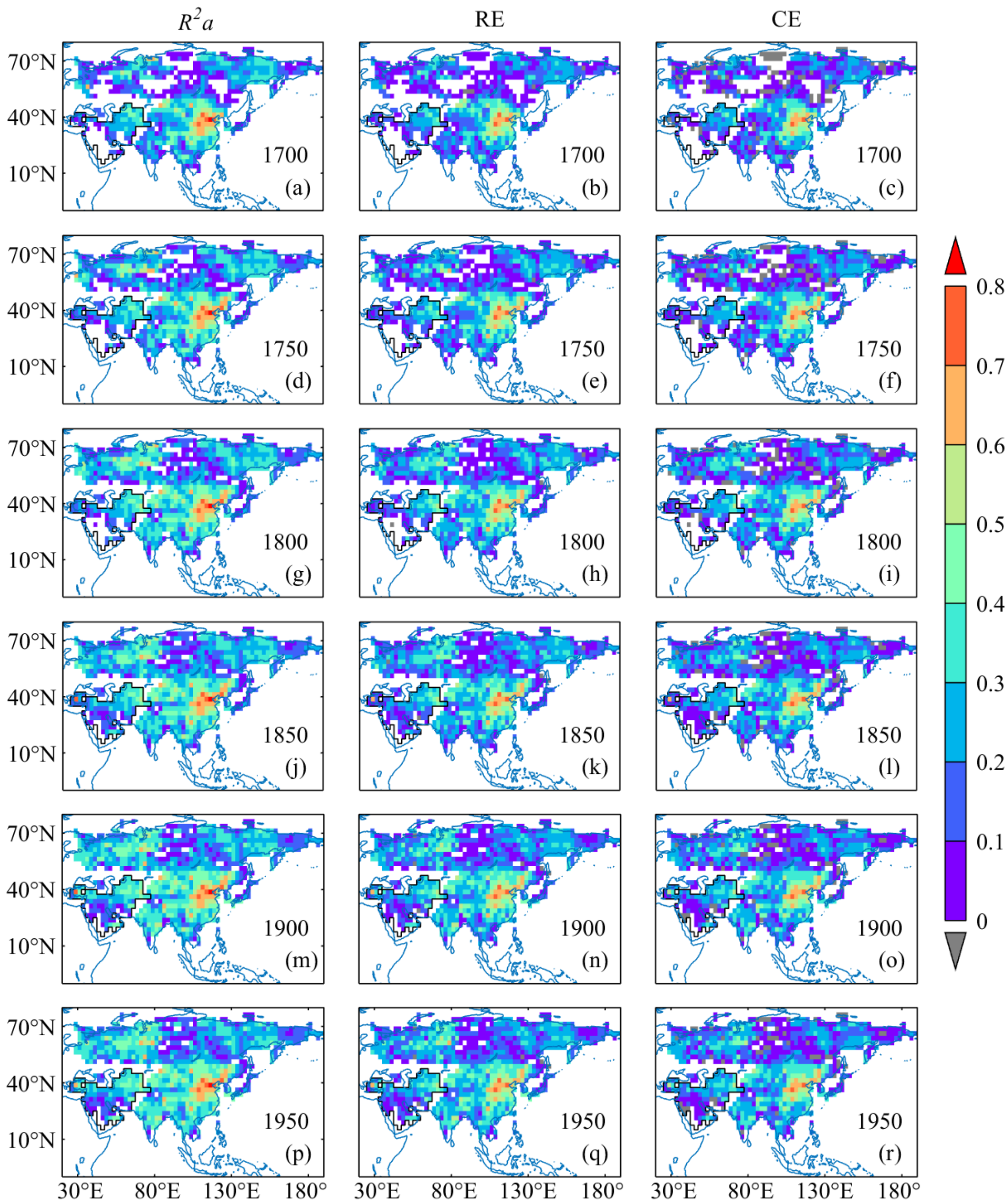

Figure 7: R^2a, RE, and CE for wet season SPI reconstruction by multi-proxies without using tree-ring density chronologies and width chronologies with negative correlations to precipitation, the black line indicates the boundary of the region in which the wet season is Nov-Apr as that in Fig. 1.

https://doi.org/10.5194/essd-2022-200
Preprint. Discussion started: 1 September 2022

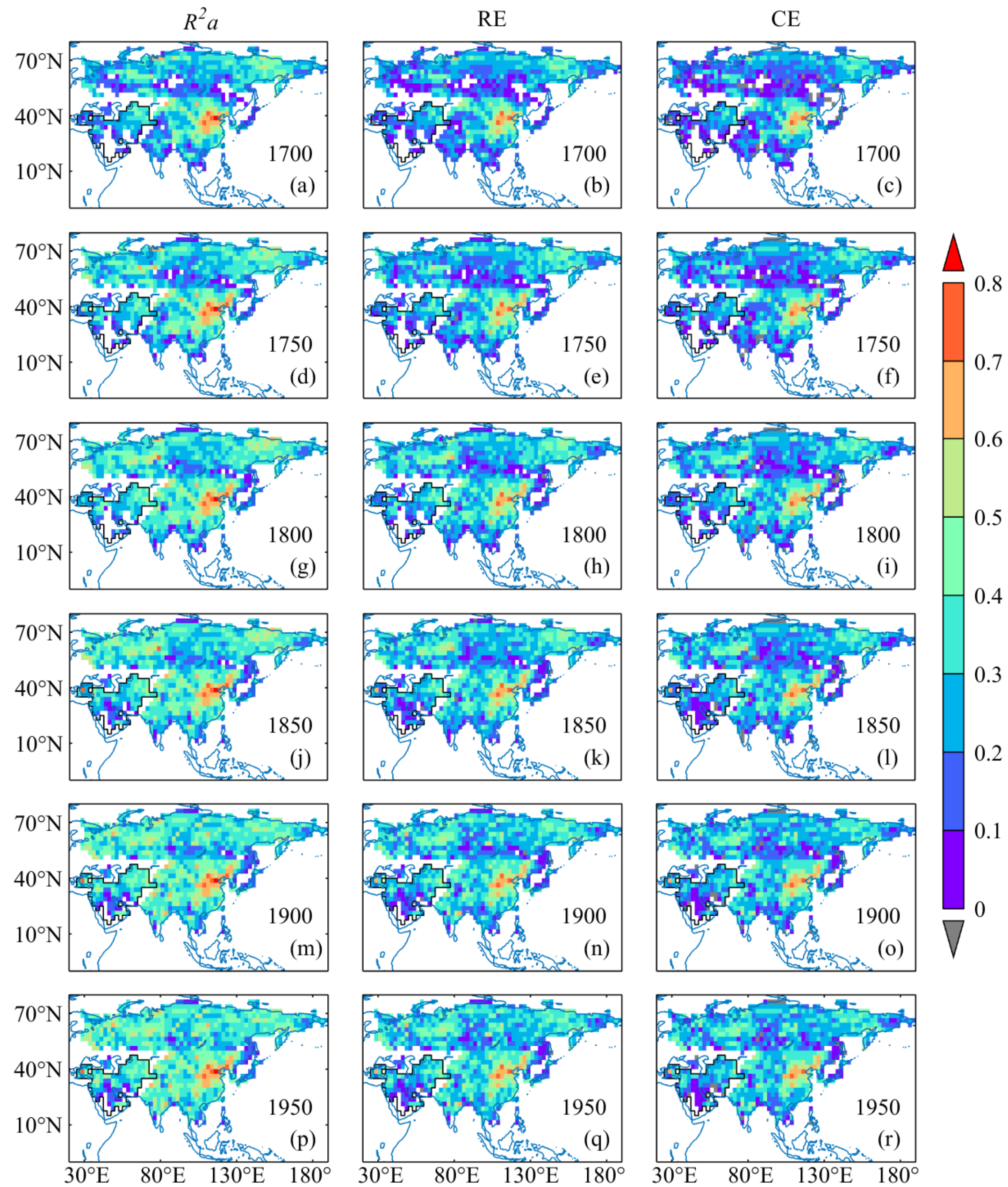

Figure 8: R^2a, RE, and CE for wet season SPI reconstruction by multi-proxies including tree-ring density chronologies and width chronologies with negative correlations to precipitation, the black line indicates the boundary of the region in which the wet season is Nov-Apr as that in Fig. 1.

https://doi.org/10.5194/essd-2022-200
Preprint. Discussion started: 1 September 2022

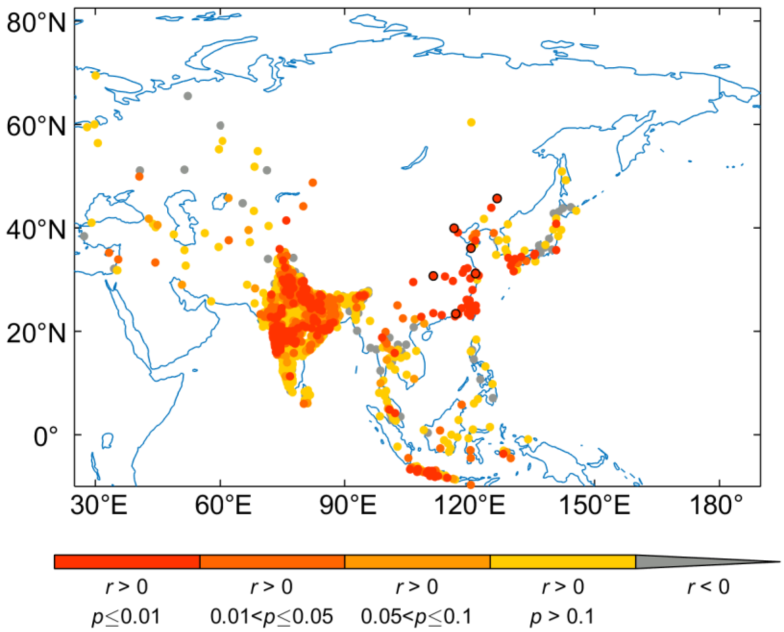

Figure 9: Correlations between Nov-Oct precipitation anomaly percentage for weather stations with at least 30-year records before 1948 from GHCMm and Nov-Oct SPI reconstruction in corresponding grids. The six selected sites in eastern China are shown with black edges, and the comparisons between observation and reconstruction year by year in these sites will be shown as the examples in Fig. 10.

https://doi.org/10.5194/essd-2022-200
Preprint. Discussion started: 1 September 2022

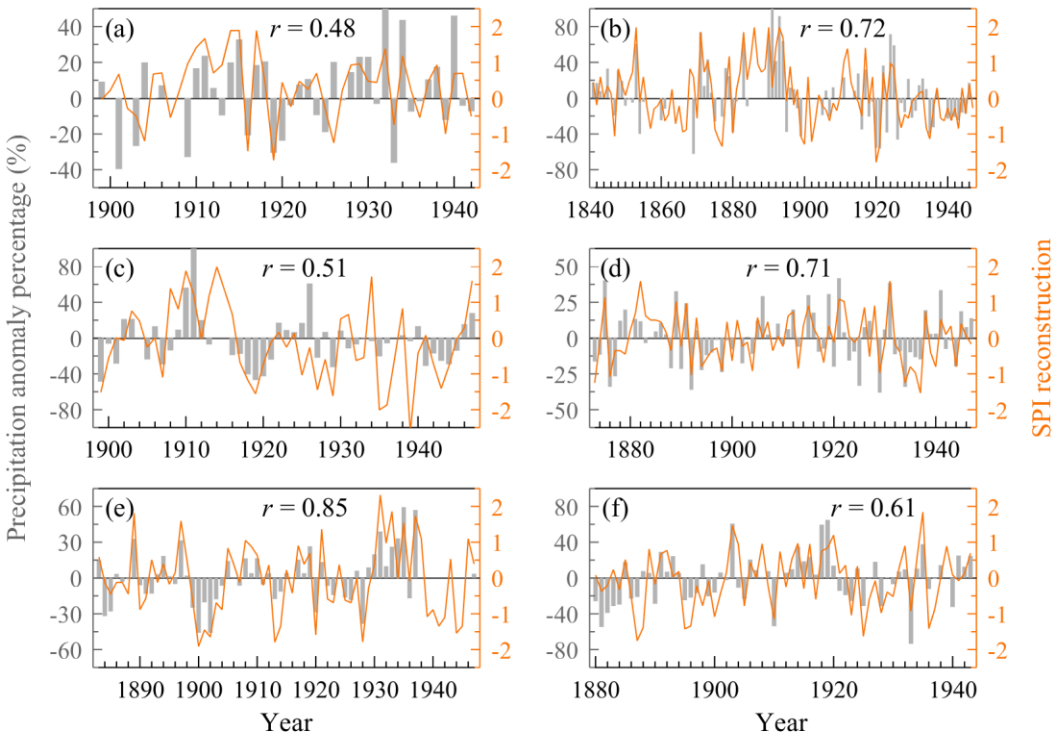

Figure 10: Comparisons between Nov-Oct precipitation anomaly percentage for 6 sites across eastern China from Tao et al. (1997) and Nov-Oct SPI reconstruction in corresponding grids. (a) Haerbin (126.62 °E, 45.68 °N), (b) Beijing (116.28 °E, 39.93 °N), (c) Qingdao (120.33 °E, 36.07 °N), (d) Shanghai (121.43 °E, 31.17 °N), (e) Yichang (111.30 °E, 30.70 °N), and (f) Shantou (116.68 °E, 23.40 °N). Their locations are also shown in Fig. 9.